Journal of The Electrochemical Society, **159** (9) D512-D517 (2012)
0013-4651/2012/159(9)/D512/6/$28.00 © The Electrochemical Society

Growth Mechanism of Self-Assembled TiO_2 Nanorod Arrays on Si Substrates Fabricated by Ti Anodization

Yung-Huang Chang, Hsiao-Wei Lin, and Chih Chen[z]

Department of Materials Science and Engineering, National Chiao-Tung University, Hsinchu 30010, Taiwan

The growth rate and the growth mechanism are investigated by examining the results of scanning electron microscope (SEM) and X-ray photoelectron spectroscopy (XPS) on TiO_2 nanorods fabricated in the second anodization process through the nanopores of anodic aluminum oxide. Due to the strong electric field of 1.86 GV/m to 1.33 GV/m, the average ultra-fast growth rate of 250 nm/s is observed, and the abrupt increase of height reaches to 85.2% of its destined height in the early growth stage of 0.6 s. Then the growth rate decreases when the electric field decays with the increase of height, and it is interrupted by the dielectric breakdown under an electric field of 0.65 GV/m. According to the XPS analyzes, the TiO_2 species on the outer shell of nanorods are observed, and the sub-oxides, Ti_2O_3 and TiO, are exhibited after Ar^+ ions sputtering. It is proposed that the bottom growth mechanism is identified by the analyzes upon SEM and XPS results.
© 2012 The Electrochemical Society. [DOI: 10.1149/2.034209jes] All rights reserved.

Manuscript submitted March 2, 2012; revised manuscript received June 19, 2012. Published August 14, 2012.

Anodic metal oxide nanostructures fabricated by a chemical anodization process through AAO template have attracted considerable attention in recent years.[1–7] Since Shimizu and co-workers investigated anodic tantalum oxide in the 90 s,[8] the metals such as Ta, Nb, Ti, and W have been studied.[9–26] Due to the unique nanostructures, physical characteristics, and chemical stability, the metal oxides can be developed as field emitters,[3,4,21] nanocapacitors,[13,14] optoelectronic devices,[6,20] and biomaterials.[24]

The surface morphology, ions transport, and growth mechanism of anodic metal oxide nanostructures has been investigated. Shimizu et al. indicated that the needle-like inner metal oxide would penetrate into the outer metal oxide if the inner metal oxide owns a lower ionic resistivity than the outer metal oxide.[8] The literatures pointed out that the diameter and density of anodic metal oxides are controlled by controlling the morphology of anodic aluminum oxide (AAO) template in the first anodization process,[25,27,28] and the growth height is enhanced by adding the voltage during the second anodization process. Furthermore, the ions transport mechanism of Ta_2O_5, Nb_2O_5, and WO_3 nanostructures was investigated, and the results specified that actions not only migrate in metal oxide but also penetrate into the outer AAO wall.[5,7,13] The two growth sources for Ta_2O_5[13] and WO_3[7] at both the electrolyte/metal oxide interface and the metal oxide/metal interface were proposed. In addition to the assistance of AAO template for TiO_2 nano-structure architectures in an anodization process, Ti metal material was directly used to fabricate tubular nanostructures in electrolytes containing fluorides.[29–31] However, few ones show great regards to the growth rate of anodic TiO_2 nanorods fabricated in the second anodization and the termination of growth along AAO nanopores by the interruption of dielectric breakdown.[32] In addition, although the growth mechanism and ion transport of anodic Ta_2O_5, Nb_2O_5, and WO_3 nanostructures have been reported,[5,7,13] the growth mechanism and ion transport of TiO_2 nanorods fabricated in the second anodization are rarely studied.[33] Therefore, there are still some situations needed to be confirmed for anodic TiO_2 nanorods.

In this study, we used an Al/Ti superimposed metal layer on substrate to fabricate TiO_2 nanorods through the nanoporous channels of AAO template in 0.3 M oxalic acid electrolyte during two-step anodization process. The ultra-fast growth rate and dielectric breakdown field strength are investigated from SEM results. The ions transport, growth rate, and nanostructures are investigated for anodic TiO_2 nanostructures to study the growth mechanism. A model of growth mechanism of anodic TiO_2 nanostructures was proposed to explain the ions distribution and ions transport.

Experimental

To fabricate anodic TiO_2 nanorods, first, a Ti film of 130 nm was deposited on a P-type (100) silicon substrates by an e-gun evaporation system. Subsequently, a 700 nm Al film was deposited by a thermal evaporation coater. In order to control the morphology of anodic TiO_2 nanorods, a two-step anodization process was fulfilled on the Al/Ti films, as shown in Fig. 1a.[25] The first anodization carried out in a 0.3 M oxalic acid ($H_2C_2O_4$) electrolyte was applied by a 40 V bias at room temperature until the current dropped down to 1 mA. A highly ordered nanoporous AAO structure were fabricated during this period, and then regular TiO_2 nanodot arrays have grown to 91% height and penetrated into AAO. The as-prepared AAO possessed an average diameter of about 20 nm, a pore distance of about 95 nm, a height of about 900 nm and the nanopores have an aspect ratio of 45. Then the second anodization process was performed in the same condition except the bias, so that various heights of TiO_2 nanorod arrays can be prepared. Due to the equipment limitation of Keithley 2400 sourcemeter, the largest voltage of 117 V is provided. After the two-step anodization process, nanoporous AAO film was selectively removed by wet chemical etching at 60°C in a mixed solution, 6 wt% phosphoric acid (H_3PO_4) and 1.8 wt% chromic acid ($H_2Cr_2O_4$), for 20∼40 min. Therefore, TiO_2 nanorod arrays can be exhibited on the Si substrate after selective removal of AAO. This approach can produce self-aligned and height-controlled TiO_2 nanorods on a Si substrate.

The current characteristics of all samples were recorded using a keithley 2400 sourcemeter. Surface morphology of the TiO_2 arrays was examined by a field-emission scanning electron microscope (FE-SEM, JSM-6500F). XPS was performed by an ESCA PHI 1600 system with a monochromatic Al Ka source and a charge neutralizer.

Results and Discussion

The SEM image in Fig. 1b showed the surface morphology of the nanostructures with AAO removal when the first anodization process was terminated as soon as the current started to drop down, labeled as 1 in Fig. 1a. Due to the roughness of AAO, the anodizing time for the barrier layer of AAO to touch underlying Ti layer is quiet different, so that various kinds of anodizing results are observed: nanodots, root-like nanostructures, and even unanodizing Ti metal. The residual Al metal is also found as shown by the arrow. To terminate current in the middle, labeled as 2 in Fig. 1a. Although most nanodots have been fully grown, some unripe nanodots, root-like nanostructures, and even Ti metal are still found in Fig. 1c. It is because ionic current prefers to migrate in the titanium oxide with lower ionic resistivity than the aluminum oxide, therefore growth at another situation will not start until the fabricated nanodots have been completed.[7] When the current approaches 1 mA, the whole nanodots have been fabricated, as shown in Fig. 3a.

The re-growth of nanodots structure converted to nanorods was carried out by using enlarged voltage to control the height in a second anodization process. Figure 2a to 2c represent the cross-sectional SEM images of the TiO_2 nanorods fabricated in a second anodization

[z]E-mail: chih@cc.nctu.edu.tw

Downloaded on 2014-04-28 to IP 140.113.38.11 address. Redistribution subject to ECS terms of use (see ecsdl.org/site/terms_use) unless CC License in place (see abstract).

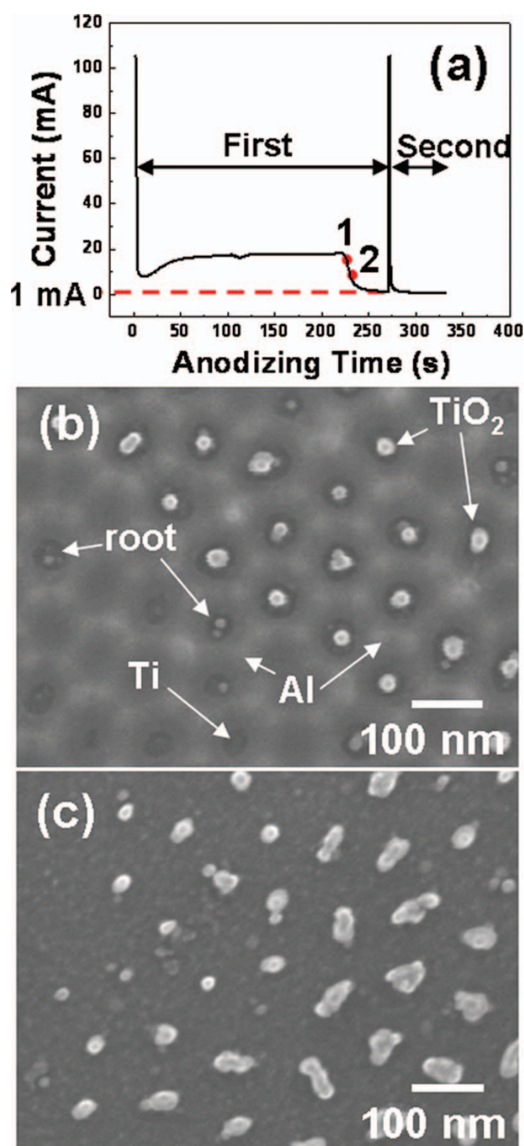

Figure 1. (a) The current diagram showing the two-step anodization process: the oxidation of Al metal and Ti metal. Plan-view SEM images of (b) and (c) showing the nanostructures with AAO removal when the first anodization process was terminated at red label 1 and 2 in (a), respectively.

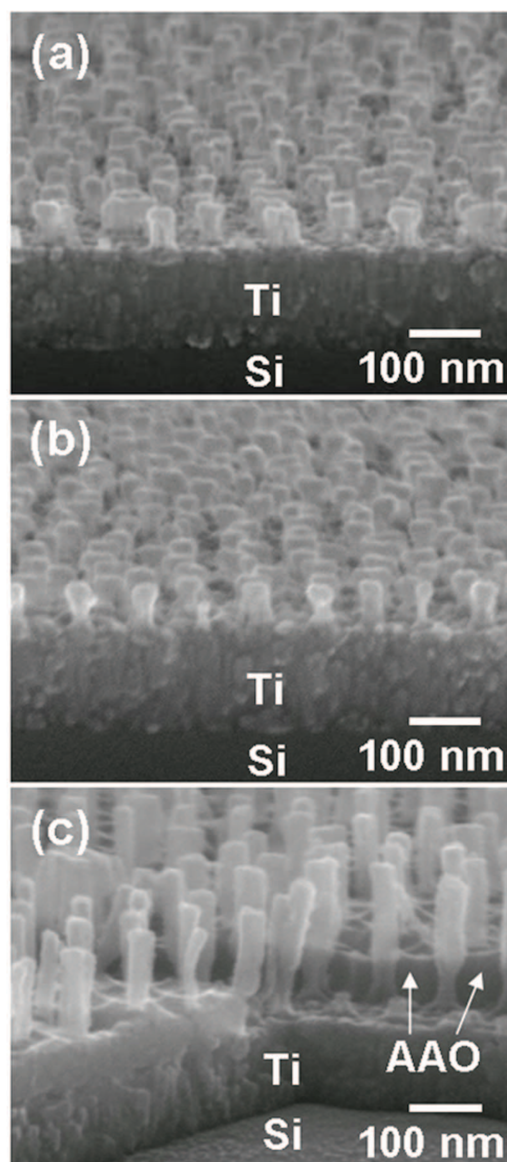

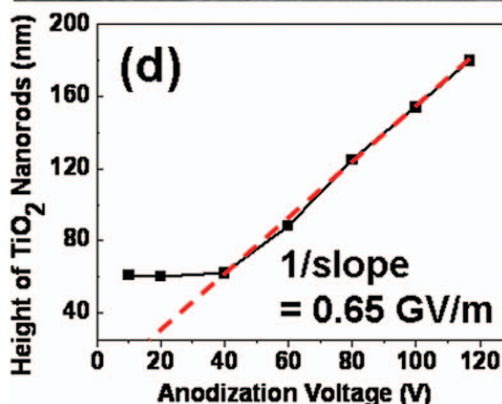

Figure 2. Cross-sectional SEM images showing TiO_2 nanorods fabricated in the second anodization process at (a) 10 V, (b) 40 V, and (c) 117 V for 240 s. (d) The plot of the measured height for the TiO_2 nanorods against various anodization voltages. The AAO template was removed completely in (a) and (b), however, the residual AAO was still observed in (c) after the selective etching.

process at 10 V, 40 V and 117 V for 240 s, whose height is 62 nm, 63 nm, and 182 nm, respectively. Figure 2d plots the average height of the TiO_2 nanorods against the second anodization voltage. It is found that the height of TiO_2 nanorods does not change apparently from 10 V to 40 V, yet it rises abruptly from 60 V to 117 V. The dielectric breakdown field strength[32] of 0.65 GV/m calculated from 60 V to 117 V limits the growth height of nanorods. No evident signs of growth were found as the field strength was below this value. For instance, the height of nanodots fabricated at 40 V was not further enhanced when the second anodization process at 10 V was performed under the field strength of 0.16 GV/m. In other words, the nanorods would not grow below the dielectric breakdown electric field strength of 0.65 GV/m.

It is intriguing that the growth of TiO_2 nanorods almost reached saturation in a very short time. Figures 3a through 3c depict the cross-sectional SEM images of the TiO_2 nanorods fabricated in a re-growth procedure at 117 V for 0 s, 0.6 s, and 60 s, respectively. The mean heights are 63 nm, 155 nm, and 181 nm for the three growth conditions. Figure 4a illustrates the measured height of the TiO_2 nanorods at various growing time. The abrupt increase of height

Downloaded on 2014-04-28 to IP 140.113.38.11 address. Redistribution subject to ECS terms of use (see ecsdl.org/site/terms_use) unless CC License in place (see abstract).

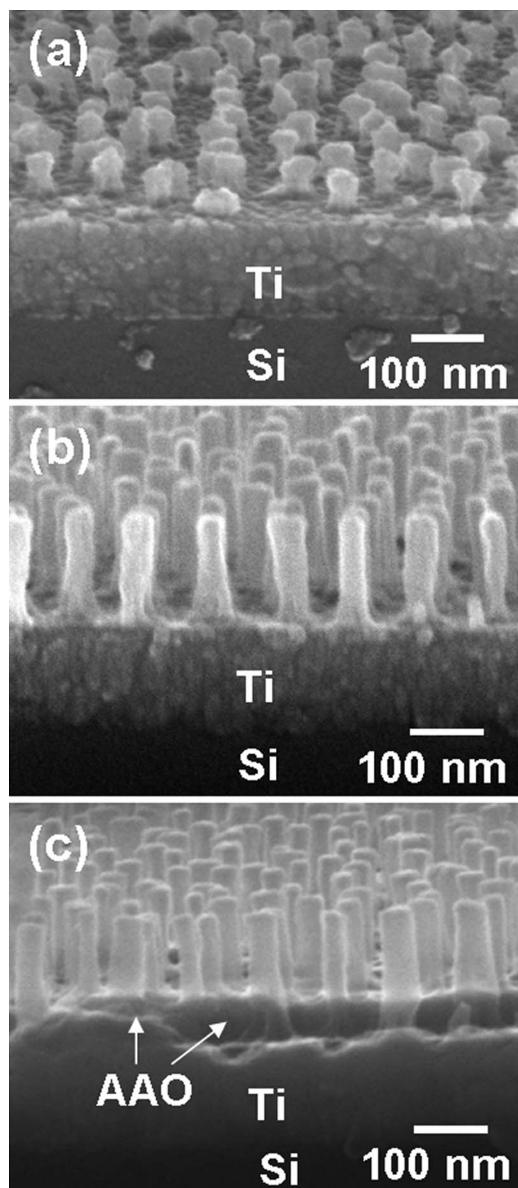

Figure 3. Cross-sectional SEM images showing TiO_2 nanorods fabricated in the second anodization process at 117 V for (a) 0 s, (b) 0.6 s, and (c) 60 s. The AAO template was removed completely in (a) and (b), however, the residual AAO was still observed in (c) after the selective etching.

is found clearly in the early growth stage and appears within 0.6 s to 85.2% of height. Then the height reaches plate situation, and no apparent signs of growth were found. Figure 4b shows the time-dependent growth rate curve and electric field strength. The average 250 nm/s ultra-fast growth rate calculated from 63 nm to 88 nm within 0.1 s is observed within a strong electric field of 1.86 GV/m to 1.33 GV/m. However, it drops abruptly to approximately 0.79 nm/s in an electric field of 0.68 GV/m in 3.1 s, and almost approaches non-growth in a 0.65 GV/m electric field after 15 s. The strong electric field of 1.86 GV/m applied in the fabrication process resulted in the fast growth rate of the nanorods in the early stage, and then the growth rate decreases due to the decayed electric field with the increase of height. Consequently, the nanorods keep on growing along the AAO nanopores until the growth rate is interrupted by the dielectric breakdown within the electric field strength of 0.65 GV/m. In other words, the nanorods start to grow as the electric field strength is lager than the one of dielectric breakdown.

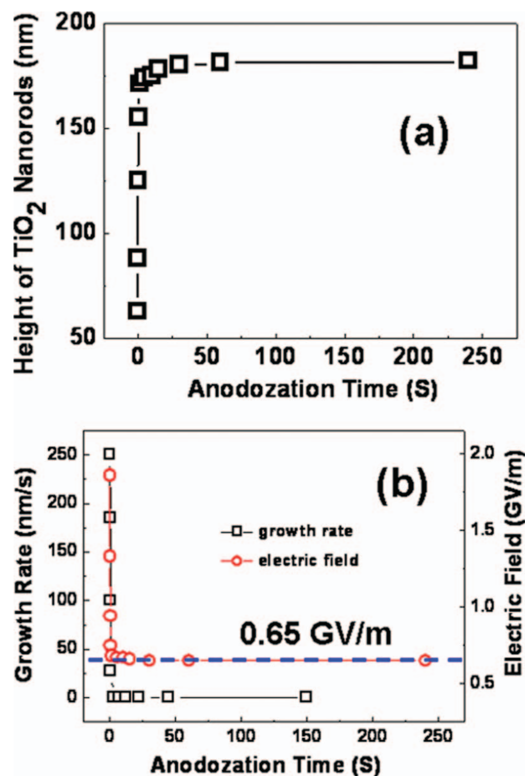

Figure 4. (a) The height of the TiO_2 nanorods fabricated in the second anodization process at various anodization times. The height almost reaches saturation within 1 s. (b) The plots of growth rate and electric field at various anodization times for TiO_2 nanorods.

To investigate the growth mechanism of TiO_2 nanorods by anodic oxidation, the root structure of the nanorods was examined. After the desired anodization time, the AAO template was removed. Then the TiO_2 nanorods were removed by ultrasonic, so that the root structure of the nanorods can be observed. Figures 5a through 5c represent the plan-view SEM images showing the root structures at 80 V for 0.5 s, 10 s, and 240 s, respectively. It is interesting that the shape of the root changes from circular to flower-like. Furthermore, the area of the root structure increases with the increase of anodization time. As highlighted in the square in Figure 5b, four TiO_2 nanorods remained on the substrate after the ultrasonic treatment. The position of the TiO_2 nanorods situates approximately in the center of the flower-like structure.

To investigate the ion transport mechanism, the survey spectra of Ti, Al, and O elements were examined by XPS on the TiO_2 nanorods with AAO removal fabricated in a 40/80 V anodization process for 10 s. All spectra were referenced to C 1 s at 284.5 eV. Then the survey spectra of Ti and O element were fitted by using Gaussian functions with a Shirley background subtraction. Due to the Ti 2p spectrum consisted of two binding energy of Ti $2p_{1/2}$ and Ti $2p_{3/2}$ located at 458.8 eV and 464.6 eV, respectively,[34,35] TiO_2 structure was confirmed, which is not shown here. Figure 6 shows the XPS Ti $2p_{3/2}$ spectra recorded with non-, 200 s, and 400 s Ar^+ sputtering, respectively, with appropriate Gaussian fitting curves. The spectrum with 400s Ar^+ sputtering can be fitted into four sub-peaks, which sub-peak 1 at 458.8 eV is associated with +4 oxidation state in TiO_2, sub-peak 2 at 457.0 eV is related to +3 oxidation state in Ti_2O_3, sub-peak 3 at 455.2 eV is connected to +2 oxidation state in TiO, and sub-peak 4 at 454.1 eV is linked to neutral oxidation state in Ti metal, as shown in Fig. 6a.[35–37] The XPS result for unsputtering sample in Fig. 6c shows only titanium dioxide on the surface of TiO_2 nanorods without other sub-oxides. However, with the increase of sputtering time, the sub-oxides, Ti_2O_3 and TiO, are gradually exhibited. Ti metal with neutral

Downloaded on 2014-04-28 to IP 140.113.38.11 address. Redistribution subject to ECS terms of use (see ecsdl.org/site/terms_use) unless CC License in place (see abstract).

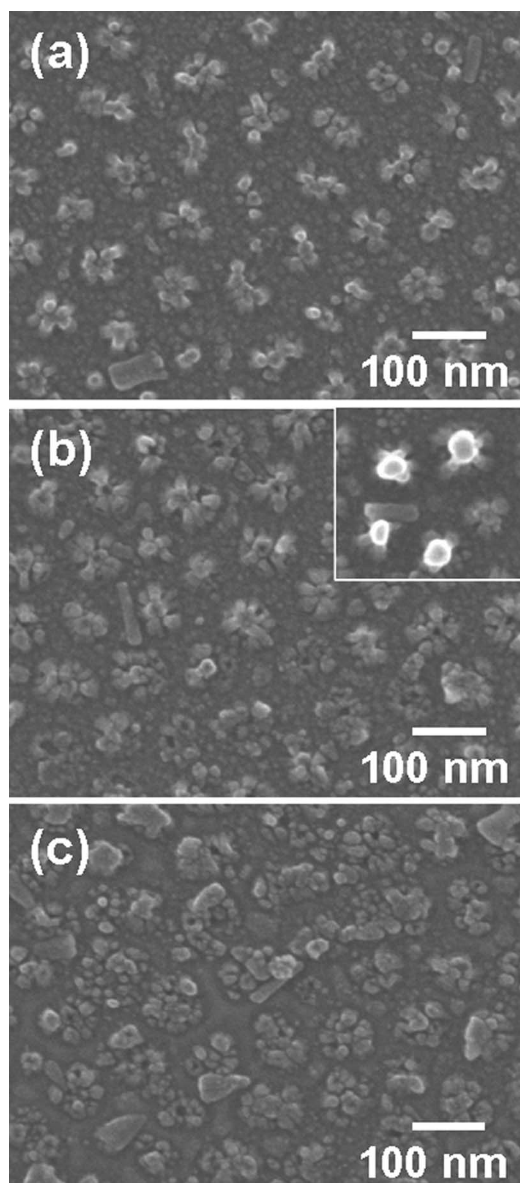

Figure 5. Plan-view SEM images showing the root structures of the TiO_2 nanorods fabricated in the second anodization process for (a) 0.5 s, (b) 10 s, and (c) 240 s after they were removed by ultrasonic vibration. The AAO template has been removed completely.

oxidation state observed in spectra was resulted from the underlying Ti layer because of the unpreferential Ar^+ ion bombardment on the sample that not only shortened the TiO_2 nanorods but also etched the gaps between nanorods. Besides, only the TiO_2 species without the other sub-oxides were also examined on the outer shell of the TiO_2 nanorods fabricated in the second anodization for 0 s, 0.1 s, and 0.6 s, as schematically shown in Fig. 9.

The XPS O 1 s spectrum measured on unsputtering specimen with fine Gaussian fitting curves is shown in Fig. 7a. The spectrum can be assigned into three sub-peaks, with sub-peak 1 and sub-peak 2 located at 530.4 eV and 531.8 eV, both being associated with oxygen species O^{2-} in TiO_2 and Al_2O_3,[5,7,33,38] respectively. Sub-peak 3 with binding energy of 533.4 eV could be attributed to absorbed oxygen on the surface.[38] Sub-peak 3 would not be found after Ar^+ sputtering process, that is, oxygen absorbed on the surface is confirmed further and is eliminated with the removal of surface material. Oxygen species related to TiO_2 and Al_2O_3 are still observed after Ar^+ sputtering process. The Al 2p spectrum recorded on unsputtering specimen in

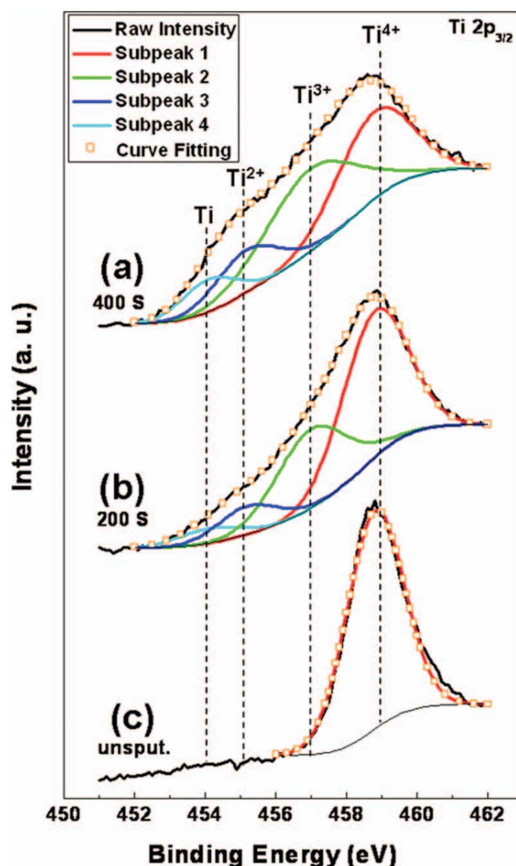

Figure 6. Ti $2p_{3/2}$ XPS spectra for TiO_2 nanorods fabricated in the second anodization process at 80 V for (a) non-, (b) 200 s, and (c) 400 s sputtering time. The results were recorded with the removal of AAO template.

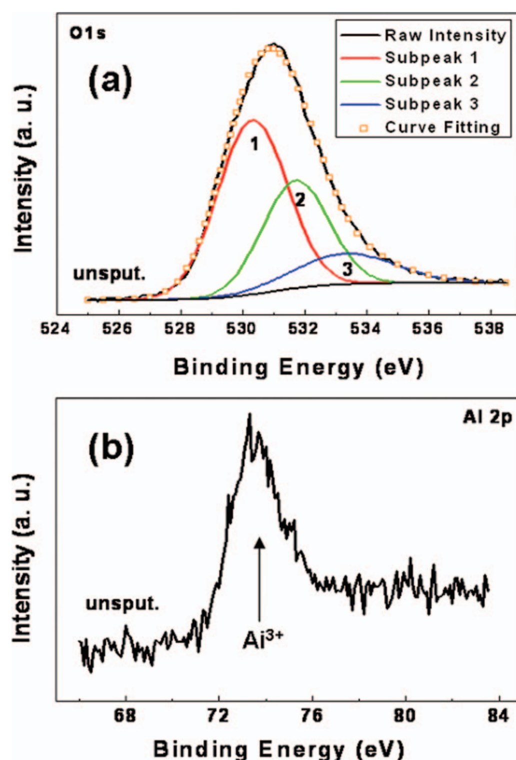

Figure 7. (a) O 1 s, and (b) Al 2p XPS spectra for TiO_2 nanorods fabricated in the second anodization process at 80 V without sputtering. The results were recorded with the removal of AAO template.

Downloaded on 2014-04-28 to IP 140.113.38.11 address. Redistribution subject to ECS terms of use (see ecsdl.org/site/terms_use) unless CC License in place (see abstract).

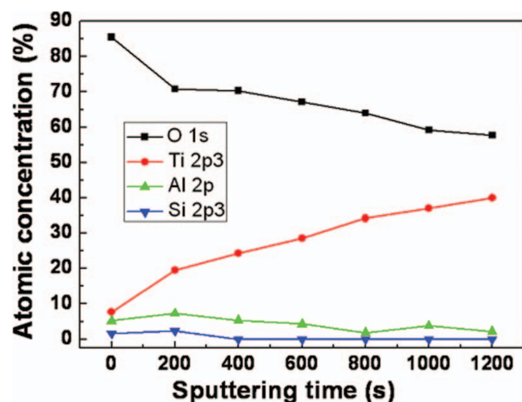

Figure 8. XPS atomic concentrations depth profiles for TiO_2 fabricated in the second anodization process at 80 V for 10 s. The results were recorded with the removal of AAO template.

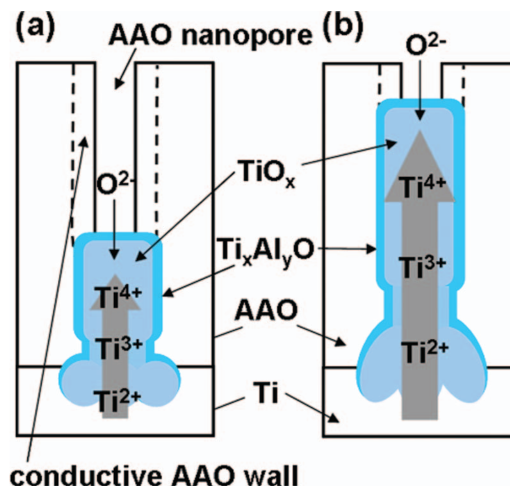

Figure 9. Schematic diagram showing the growth mechanism of TiO_2 fabricated (a) at the terminated current of 1mA, and (b) in the second anodization for extended time. The arrows show the ions transport process during the anodization.

Fig. 7b shows a symmetrical peak which is associated with oxidized Aluminum Al^{3+} in Al_2O_3 at the binding energy of 74.5 eV.[5,13] Aluminum species related to Al_2O_3 can still be observed after Ar^+ sputtering process. Whether sputtering or not, no peak related to Al metal with binding energy of 72.1 eV was presented in the spectrum.[5,13] In other words, the outer Al metal layer is fully anodized to become Al_2O_3 during the anodization process.

The XPS depth profiles for atomic concentrations of the main elements were explored on the AAO-free TiO_2 nanorods sample with Ar^+ sputtering, as shown in Fig. 8. When at 6.62, the ratio of oxygen to titanium and aluminum atoms, O:(Ti + Al), is maximum on the surface without Ar^+ sputtering. Then it decays to 2.65 after 200 s Ar^+ sputtering, and further decreases to 1.37 after 1200 s Ar^+ sputtering. The ratio of 6.62 is extremely larger than the O:Ti atoms ratio of 2 in TiO_2 and the O:Al atoms ratio of 1.5 in Al_2O_3. The oxygen-rich phenomenon on the surface of TiO2 nanorods could be a result of the absorbed oxygen, nonstoichiometric oxygen (action vacancies, interstitial oxygen), bounder water, and incorporated oxygen-containing ions.[7,13] The lower ratio of 1.37 resulted from shortened TiO_2 nanorods after 1200 s Ar^+ sputtering is attributed to the presentation of Ti_2O_3 and TiO with a lower ratio of 1.5 and 1.0, respectively, even to the contribution of Ti metal. The Al element was always perceived in the XPS profiles spectra during the Ar^+ sputtering process. However, the Al atoms concentration of 5.20% at the surface gradually decreases to 2.24% as Ar^+ sputtering time increases to 1200 s. This is resulted from the thinning on the wall of nanorods due to the imperfectly unpreferential Ar^+ ion bombardment, that is, Al element mainly presents in the outer part of nanorods.[7,13] The concentration of Si atoms is below 2.4% at the top of nanorods and with the shortening on nanorods, decays are negligible after the sputtering of 400 s. Lee et al. pointed out that SiO_2 nanoparticles were formed at the top of nanopillars during anodization process because Si atoms at the Ti/Si interface were oxidized and converted into Si ions to migrate toward the top of nanopillars.[23]

The average diameter of the AAO pores is approximately 20 nm fabricated at 40 V, however, the mean diameter is 45 nm for the nanorods in Fig. 2 and 3. Like the growth mechanism of anodic Ta_2O_5 and WO_3 nanorods,[7,13] due to the thicker diameter of nanorods compared with AAO nanopores, and the presentation of Al^{3+} species in the outer part of nanorods, it is implied that the penetration behavior of Ti ions in the outer part of the AAO cell walls occurs during the anodization process. Besides, the outer part of the AAO cell walls is considered as a low ionic resistivity region due to physical defects, cation vacancies, anionic species, and bound water.[7,13] Furthermore, because there has been no exceeding quantity of 7.3% for Al element and Ti species in TiO_2 observed at the surface of TiO_2 nanorods, it involved that Al-O bonds in the outer part of the AAO cell walls dissociate under the field, so that O^{2-} ions could participate continuously in the anodiztion process with adjacent oxidized titanium, and most of the Al^{3+} ions were expelled in the electrolyte and a few ones were injected into the growth.[7,13] Therefore, Ti and oxygen ions migrate there and react with dissociated O^{2-} ions and Al^{3+} ions to result in the formation of Ti_xAl_yO (mixed TiO_2 and Al_2O_3) in the outer shell of the nanorod, as schematically shown in Fig. 9b.

When a high voltage was applied, the underling Ti layer is ionized and starts to migrate outward to the top of the nanorod under the field. Meanwhile, oxygen ions migrate inward to the bottom. From the results of XPS analysis mentioned before, the distribution of oxidized titanium is confirmed that TiO_2 is mainly located at the top of nanorods, Ti_2O_3 at the middle, and TiO at the bottom, respectively, as shown in Fig. 9. Therefore, the area of sub-band 1 (Ti^{4+}) for unsputtering sample decays with the increase of sputtering time. On the other hand, the increase of the signals for sub-band 2 (Ti^{3+}) and sub-band 3 (Ti^{2+}) is observed, as shown in Fig. 6. On the basis of the above results, the following mechanism is proposed to explain the growth of the TiO_2 nanorods: ionized Ti drift from underling Ti layer toward the top of nanorod, and is continuously oxidized to increase their oxidation state of Ti^{2+} to Ti^{4+} during the traveling until the dielectric breakdown interrupts the growth. Besides, due to the fact that TiO_2 species on the outer shell were exhibited not only in the nanorods but also in the nanodots, we can see how sub-oxides were revealed after sputtering etching. Plus as time increased, the root-like nanostructures were enlarged, we can thus infer that the growth point is under the bottom rather than the TiO_2/electrolyte interface.

Conclusion

In summary, we studied the growth mechanism in TiO_2 nanorods fabricated by two-step anodic oxidation. The abrupt increase of height appears to be 85.2% height within 0.6 s in the early growth stage. The average ultra-fast growth rate of 250 nm/s is observed under a strong electric field of 1.86 GV/m to 1.33 GV/m in 0.1 s, and it drops abruptly to 0.79 nm/s with an electric field of 0.68 GV/m in 3.1 s. The growth mechanism is interrupted and almost approaches non-growth by the dielectric breakdown with an electric field of 0.65 GV/m after 15 s. The TiO_2 species on the outer shell are examined not only in the nanorods but also in the nanodots, and the signals of the sub-oxides, Ti_2O_3 and TiO, are gradually exhibited after Ar^+ ions sputtering. The distribution of oxidized titanium has pointed out that TiO_2 is mainly located at the top of nanorods, Ti_2O_3 at the middle, and TiO at the bottom. The bottom growth mechanism is confirmed by the analyzes upon SEM and XPS results.

Downloaded on 2014-04-28 to IP 140.113.38.11 address. Redistribution subject to ECS terms of use (see ecsdl.org/site/terms_use) unless CC License in place (see abstract).

Acknowledgments

The authors thank the National Science Council of the Republic of China, Taiwan, for the financial support in this research under Contract No. NSC 98-2221-E-009-036-MY3.

References

1. S. H. Jeong, Y. K. Cha, I. K. Yoo, Y. S. Song, and C. W. Chung, *Chem. Mater.*, **16**, 1612 (2004).
2. I. H. Park, J. W. Lee, and C W Chung, *J. Ind. Eng. Chem.*, **11**, 590 (2005).
3. T. M. Chen, F. M. Pan, J. Y. Hung, L. Chang, S. C. Wu, and C. F. Chen, *J. Electrochem. Soci.*, **154**, D215 (2007).
4. T. M. Chen, J. Y. Hung, F. M. Pan, L. Chang, J. T. Sheu, and S. C. Wu, *J. Electrochem. Soci.*, **11**, K40 (2008).
5. A. Mozalev, M. Sakairi, I. Saeki, and H. Takahashi, *Electrochimica Acta*, **48**, 3155 (2003).
6. S. Z. Chu, S. Inoue, K. Wada, S. Hishita, and K. Kurashima, *J. Electrochem. Soci.*, **152**, B116 (2005).
7. A. Mozalev, V. Khatko, C. Bittencourt, A. W. Hassel, G. Gorokh, E. Llobet, and X. Correig, *Chem. Mater.*, **20**, 6482 (2008).
8. P. Skeldon, K. Shimizu, G. E. Thompson, and G. C. Wood, *Philos. Mag., B*, **61**, 927 (1990).
9. A. I. Vorobyova and E. A. Outkina, *Thin Solid Films*, **324**, 1 (1998).
10. A. I. Vorobyova, V. A. Sokol, and E. A. Outkina, *Appl. Phys. A*, **67**, 487 (1998).
11. A. Mozalev, A. Surganov, and S. Magaino, *Electrochimica Acta*, **44**, 3891 (1999).
12. A. Mozalev, M. Sakairi, I. Saeki, and H. Takahashi, *Electrochimica Acta*, **48**, 3155 (2003).
13. A. Mozalev, M. Sakairi, and H. Takahashi, *J. Electrochem. Soci.*, **151**, F257 (2004).
14. A. Mozalev, G. Gorokh, M. Sakairi, and H. Takahashi, *J. Mater. Sci.*, **40**, 6399 (2005).
15. C. T. Wu, F. H. Ko, and C. H. Lin, *Appl. Phys. Lett.*, **90**, 171911 (2007).
16. J. Gong, W. H. Butler, and G. Zangari, *J. Mater. Chem.*, **18**, 1741 (2008).
17. I. H. Park, J. W. Lee, S. H. Jeong, and C. W. Chung, *Electrochem. Solid. State. Lett.*, **8**, C117 (2005).
18. N. I. Tatarenko and A. M. Mozalev, *Solid-State Electro.*, **45**, 1009 (2001).
19. P. L. Chen, C. T. Kuo, T. G. Tsai, B. W. Wu, C. C. Hsu, and F. M. Pan, *Appl. Phys. Lett.*, **82**, 2796 (2003).
20. S. Z. Chu, S. Inoue, K. Wada, S. Hishita, and K. Kurashima, *Adv. Funct. Mater.*, **15**, 1343 (2005).
21. P. L. Chen, W. J. Huang, J. K. Chang, C. T. Kuo, and F. M. Pana, *Electrochem. Solid. State. Lett.*, **8**, H83 (2005).
22. Y. Lei, W. Cai, and G. Wilde, *Prog. Mater. Sci.*, **52**, 465 (2007).
23. S. W. Jee, Y. W. Cho, J. M. Yang, Y. C. Park, and J. H. Lee, *J. Nanosci. Nanotechnol.*, **9**, 2603 (2009).
24. T. Sjöström, M. J. Dalby, A. Hart, R. Tare, R. O. C. Oreffo, and B. Su, *Acta Biomaterialia*, **5**, 1433 (2009).
25. T. Sjöström, N. Fox, and B. Su, *Nanotechnology*, **20**, 135305 (2009).
26. J. Oh and C. V. Thompson, *Adv. Mater.*, **20**, 1368 (2008).
27. H. Masuda and K. Fukuda, *Science*, **268**, 1466 (1995).
28. G. E. Thompson, R. C. Furneaux, G. C. Wood, J. A. Richardson, and J. S. Goode, *Nature*, **272**, 433 (1978).
29. V. Zwilling, E. Darque-Ceretti, A. Boutry-Forveille, D. David, M. Y. Perrin, and M. Aucouturier, *Surf. Interface Anal.*, **27**, 629 (1999).
30. D. Gong, C. A. Grimes, O. K. Varghese, W. C. Hu, R. S. Singh, Z. Chen, and E. C. Dickey, *J. Mater. Res.*, **16**, 3331 (2001).
31. J. M. Macak, H. Tsuchiya, L. Taveira, S. Aldabergerova, and P. Schmuki, *Angew. Chem. Int. Ed.*, **44**, 7463 (2005).
32. Y. Jeliazova, M. Kayser, B. Mildner, A. W. Hassel, and D. Diesing, *Thin Solid Films*, **500**, 330 (2006).
33. Y. H. Chang, H. W. Lin, and C. Chen, *Electrochemical and Solid-State Letters*, **14**(1), K1 (2011).
34. M. Mirshekari, R. Azimirad, and A. Z. Moshfegh, *Appl. Surf. Sci.*, **256**, 2500 (2010).
35. F. Zhang, S. Jin, Y. Mao, Z. Zheng, Y. Chen, and X. Liu, *Thin Solid Films*, **310**, 29 (1997).
36. L. Zhang, R. Persaud, and T. E. Madey, *Phys. Rev., B*, **56**, 10549 (1997).
37. A. Sandell, M. P. Andersson, M. K. J. Johansson, P. G. Karlsson, Y. Alfredsson, J. Schnadt, H. Siegbahn, and P. Uvdal, *Surf. Sci.*, **530**, 63 (2003).
38. M. H. Chan and F. H. Lu, *Thin Solid Films*, **518**, 1369 (2009).

Downloaded on 2014-04-28 to IP 140.113.38.11 address. Redistribution subject to ECS terms of use (see ecsdl.org/site/terms_use) unless CC License in place (see abstract).